MODEL-FREE FORECASTING OF LIMIT CYCLE OSCILLATIONS IN GEOMETRICALLY NONLINEAR WINGS

Cristina Riso, Amin Ghadami, Carlos E.S. Cesnik, Bogdan I. Epureanu

University of Michigan
Ann Arbor, Michigan USA
criso@umich.edu
aghadami@umich.edu
cesnik@umich.edu
epureanu@umich.edu

Keywords: nonlinear aeroelasticity, limit cycle oscillations, forecasting

Abstract: Ensuring adequate flutter margins is a critical step in aircraft design. However, geometrically nonlinear configurations may develop limit cycle oscillations even before reaching the flutter boundary. When nonlinear effects are anticipated, post-flutter analyses have to be integrated into design for preventing undesirable subcritical limit cycles. Therefore, there is a need for computationally fast post-flutter analysis methods suitable for design applications. Previous work proposed an efficient method for forecasting post-flutter responses using only a few system calculations or measurements in the pre-flutter regime. This paper applies the method for investigating the post-flutter response of a practical geometrically nonlinear wing for various design choices to demonstrate the method suitability for parametric studies.

1 INTRODUCTION

Ensuring adequate flutter margins is a critical step in aircraft design. This step is accomplished through intensive flutter computations and eventually verifications in flight test campaigns [1,2]. However, flutter margins are not a complete aeroelastic qualification metric for geometrically nonlinear configurations because limit cycle oscillations (LCOs) can arise even before reaching the flutter boundary.

Nonlinear aeroelastic effects can lead to supercritical or subcritical post-flutter responses [3]. The two scenarios are illustrated by the bifurcation diagrams in Fig. 1, which show the variation of the LCO amplitude with a control parameter (for instance, the speed or the dynamic pressure). When the post-flutter response is supercritical, LCOs smoothly arise only beyond the flutter point. This is not typically a design concern because aircraft do not operate beyond the flutter boundary. Subcritical post-flutter responses place a much more serious challenge to design. In fact, a bi-stability region exists where disturbances can suddenly cause large-amplitude LCOs.

While subcritical post-flutter response is clearly undesirable, preventing it during design is challenging. One major problem is the lack of efficient post-flutter analysis methods suitable for design space exploration [4]. Due to this shortcoming, post-flutter responses have been analyzed mostly for simple configurations such as typical aeroelastic sections or straight uniform wings. Therefore, the impact of design choices on post-flutter responses of realistic configurations is not well understood.

(a) Supercritical behavior   (b) Subcritical behavior
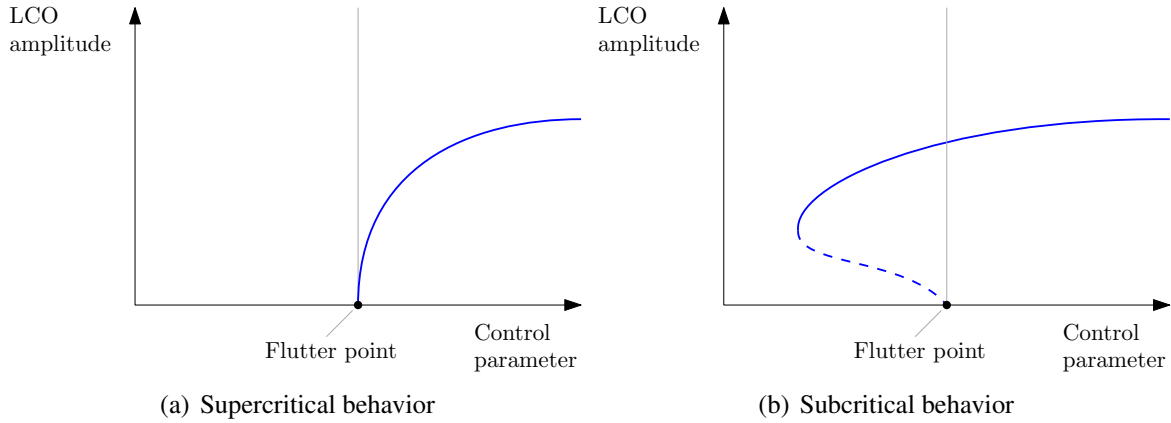
Figure 1: Possible post-flutter behaviors of a hypothetical nonlinear aeroelastic system.

Bifurcation diagrams can be computed using techniques such as time-marching schemes [5,6], harmonic balance methods [7,8], nonlinear perturbation methods [9,10], or numerical continuation methods [11]. Although these techniques are well capable of building bifurcation diagrams, they require significant theoretical or computational effort and do not scale well for complex large-dimensional models. Furthermore, some existing numerical methods may require previous knowledge of post-flutter responses to overcome convergence issues. Such limitations make existing methods impractical or not sufficiently robust for analyzing and designing realistic configurations [4].

Recently, a novel model-free method, called the bifurcation forecasting method, was proposed to forecast bifurcation diagrams of nonlinear systems using only few system outputs collected in the pre-bifurcation regime [12, 13]. Output signals can come from black-box simulations or even experimental measurements while no information of the underlying system equations is required. The method is efficient in computing bifurcation diagrams compared to alternate traditional analysis methods, and it is readily applicable to complex large-dimensional aeroelastic systems. This paper applies the bifurcation forecasting method to a practical geometrically nonlinear wing [14] and leverages the method efficiency for investigating the impact of design parameters on the wing post-flutter response. Output signals for applying the method are obtained from a low-order nonlinear aeroelastic framework, the University of Michigan's Nonlinear Aeroelastic Simulation Toolbox (UM/NAST) [14], which is treated as a black box.

The paper is organized as follows. The model-free bifurcation forecasting method is summarized in Sec. 2. The wing test case is described in Sec. 3. Numerical results for the wing post-flutter response are discussed in Sec. 4. Concluding remarks are provided in Sec. 5

2 METHODOLOGY

The post-flutter analysis method used in this paper is the model-free bifurcation forecasting method proposed in Refs. [12, 13]. The method leverages the critical slowing down (CSD) phenomenon [15] observed in nonlinear aeroelastic systems as they approach a flutter (Hopf) bifurcation. The closer the flutter point is, the longer it takes for the system to recover its initial equilibrium state after a perturbation. This means that the recovery rate decreases as a control parameter approaches its critical (flutter) value. Quantifying the CSD in the system response to perturbations allows to predict the flutter point and the post-flutter response (bifurcation diagram) while keeping the system in the pre-flutter regime.

The method presents many advantages over classical post-flutter analysis methods that make it suitable for parametric studies and design [4]. It is model free and requires only few system outputs to predict a portion of the bifurcation diagram. This eliminates the need for computationally costly parameter sweeps or complex numerical continuation schemes. Outputs can come from any black-box computational model or even from experimental measurements. This makes the method readily applicable to large-dimensional systems and even to systems for which a model is not available. Furthermore, the method characterizes the flutter type (supercritical and subcritical) and the limit cycle amplitude beyond the flutter speed which are of a great importance especially when the system operates close to the linear flutter boundary.

The main steps in the method are summarized below following the derivation reported in Refs. [12, 13]. Previous applications include structural systems [12, 16], two-dimensional typical sections with spring nonlinearities [13, 17–19], and an idealized high-aspect-ratio wing [20].

2.1 Single-Degree-of-Freedom System

To understand the method, it is convenient to consider a hypothetical single-DOF system

$$\dot{r} = f(r, U) \,, \tag{1}$$

where r is the response amplitude, U is the control parameter which is the flight speed in this study, and the overdot denotes the derivative with respect to time t.

A Taylor expansion in U about the bifurcation (flutter) point $U = \tilde{U}_F$ gives

$$\dot{r} = r \left[p(r) + \alpha_1(r)(U - \tilde{U}_F) + \alpha_2(r)(U - \tilde{U}_F)^2 + \dots \right] \,. \tag{2}$$

For parameter values close to the bifurcation, the governing equation is assumed to have such a polynomial dependence on the parameter. Note that there is no small-amplitude assumption in Eq. (2) because the expansion is in U and not in r. Mathematically, using more terms in the Taylor series approximation in Eq. (2) results in a more accurate approximation. However, using higher-order terms increases the effect of noise and uncertainties in the forecasting procedure. A first- or second-order approximation is reasonable provided that the system is close enough to the flutter speed.

Using Eq. (2), the recovery rate λ from a perturbation is introduced as

$$\lambda := \frac{d}{dt} \ln r = p(r) + \alpha_1(r)(U - \tilde{U}_F) + \alpha_2(r)(U - \tilde{U}_F)^2 + \dots \,, \tag{3}$$

where $p(r)$, $\alpha_1(r)$, $\alpha_0(r)$ are polynomial functions independent of U. These polynomials describe the variation of λ with r at a fixed U value and characterize the type of post-flutter response (subcritical or supercritical).

Based on Eq. (3), the bifurcation diagram can be predicted using few system output signals collected at pre-flutter conditions. Outputs can come from black-box simulations or experimental measurements, and can be obtained by perturbing the system with disturbances of any amplitude and type (for instance, gust loads or control-surface inputs).

The methodology is illustrated in Fig. 2. The system is perturbed at N_U conditions $U_k < \tilde{U}_F$ ($k = 1, \dots, N_U$) to collect N_r response amplitudes $r(t_j) = \tilde{r}_j$ ($j = 1, \dots, N_r$). The minimum
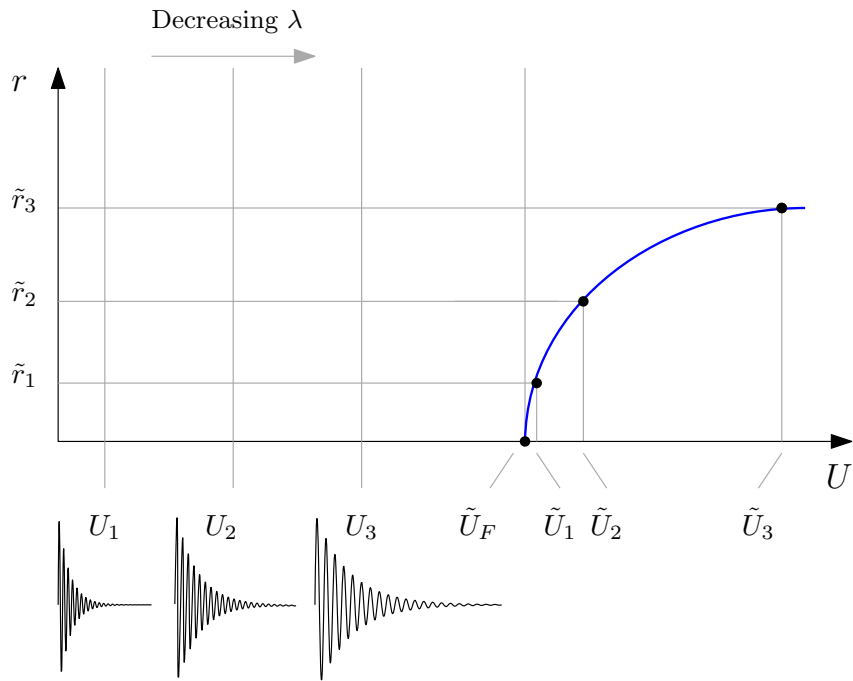
Figure 2: Schematic of bifurcation forecasting method (adapted from Ref. [20]).

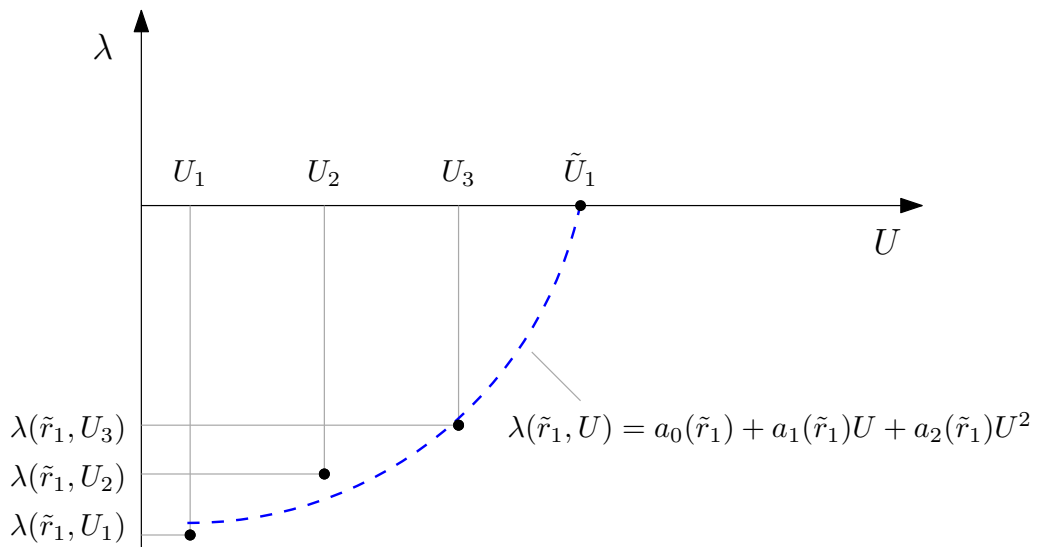$$\lambda(\tilde{r}_1, U) = a_0(\tilde{r}_1) + a_1(\tilde{r}_1)U + a_2(\tilde{r}_1)U^2$$

Figure 3: Recovery rate in the $\lambda - U$ plane at $r = \tilde{r}_1$ (adapted from Ref. [20]).

number of required measurements depends on the order of the polynomial used in Eq. (3). For example, if the recovery rate λ is approximated by a second-order polynomial in U, the method requires measurements at $N_U \geq 3$ flow speeds U. For a fixed amplitude value, for instance $\tilde{r}_1$, the recovery rates $\lambda(\tilde{r}_1, U_k) = \lambda_{1k}$ ($k = 1, \ldots, N_U$) can be computed at the various speeds as discussed below in Sec. 2.2. Once the values λ_{1k} are estimated, they are fitted in the $\lambda - U$ plane using a polynomial of the selected order (e.g., second-order) as shown in Fig. 3. The intersection between the fitting function and $\lambda = 0$ gives the value $U = \tilde{U}_1$ that identifies the point $(\tilde{r}_1, \tilde{U}_1)$ on the bifurcation diagram (see Fig. 2). In fact, points on the bifurcation diagram correspond to $\lambda = 0$, meaning that the system is at its equilibrium state. Repeating this procedure at different amplitudes gives a portion of the bifurcation diagram up to the maximum amplitude $\tilde{r}_{max}$ recorded in the output signals.

2.2 Multi-Degree-of-Freedom Oscillatory Systems

The most critical step in forecasting bifurcation diagrams is computing accurate recovery rates. Particularly, multi-DOF systems encountering flutter (Hopf) bifurcations are challenging because: 1) the system response is oscillatory; and 2) many modes are active in the response, but only one (the bifurcating mode) shows the CSD.

In flutter (Hopf) bifurcations, the system oscillates during its recovery from perturbations in the pre-flutter regime. That is because the motion is essentially two-dimensional, and one cannot use Eq. (3) for all of the points in the measured system recovery because data points adjacent to each other have different phases. Since the inertial manifold is two-dimensional, the solution is to choose a specific phase on the inertial manifold to construct a Poincaré section that reduces the system to a one-dimensional nonlinear map, and the same procedure can be used as for the non-oscillatory case to forecast the bifurcation diagram corresponding to the selected phase. To forecast the maximum amplitude of the limit cycles in the post-bifurcation regime, one has to choose local maxima of the measured system recoveries for forecasting.

Additionally, in large dimensional systems there can be several modes active in the measured system recovery. In the great majority of Hopf bifurcations, including flutter, only one pair of conjugate eigenvalues is involved in the bifurcation. Hence, the effects of the other modes can be neglected as they do not exhibit CSD and make the approximation of the recovery rates challenging. This idea is exploited in the proposed forecasting method to enhance the accuracy of bifurcation prediction. The contribution of the bifurcating mode in the response is identified and decomposed using time series analysis techniques [13, 19]. Measuring system response to perturbations, mode shapes can be estimated from system outputs directly using modal identification techniques such as the eigensystem realization algorithm (ERA) as used in Ref. [13]. Measurements are then projected onto the aeroelastic mode shapes computed at a flow speed closest to the flutter point (U_3 in Fig. 3) which provides the best approximation to the center manifold of the dynamics.

3 TEST CASE

The test case considered in this work is based on the blended-wing-body (BWB) aircraft described in Ref. [14]. This configuration is chosen due to its well-know geometrically nonlinear behavior [14] which makes it a relevant aeroelastic test case for demonstrating the forecasting method. This paper studies the half-vehicle configuration assumed as clamped at the center-line, that is, without including the interaction between the rigid-body motion and the nonlinear aeroelastic response. The full vehicle in free flight is a future target of the work.
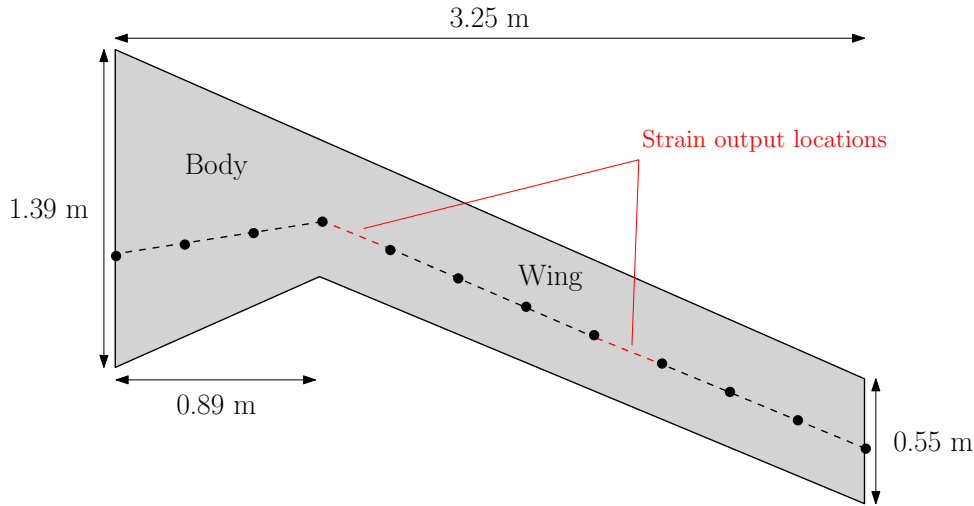
Figure 4: Test case planform and location and discretization of the UM/NAST reference beam axis (dashed line). Red segments identify elements where strain outputs are measured.

Table 1: Test case properties.

Property	Body	Wing
Reference beam axis location at root/tip (% chord)	64.38/45.60	45.60/45.60
Center of gravity location at root/tip (% chord)	64.38/45.60	45.60/45.60
Axial stiffness (N)	1.69×10^8	1.55×10^8
Torsion stiffness (Nm^2)	2.25×10^6	1.10×10^4
Out-of-plane bending stiffness (Nm^2)	7.50×10^5	1.17×10^4
In-plane bending stiffness (Nm^2)	3.50×10^7	1.30×10^5
Mass per unit span (kg/m)	50	6.20
Out-of-plane inertia per unit span (kg m)	0.70	5.00×10^{-4}
In-plane inertia per unit span (kg m)	22.00	4.62×10^{-3}

Output signals for the bifurcation forecasting are obtained by simulating wing gust responses using UM/NAST [14]. This is an integrated flight dynamic and nonlinear aeroelastic framework for simulating very flexible aircraft using a low-order geometrically exact strain-based beam formulation [21] coupled with the Peters' finite-state unsteady potential-flow theory [22] (or other aerodynamic models) and, in free-flight conditions, with the rigid-body equations. While UM/NAST is used for generating output signals and for verifying the bifurcation diagrams against time marching, the forecasting does not use any information from the UM/NAST model.

The test case planform and the location and discretization of the UM/NAST beam reference axis are shown in Fig. 4. The structural properties are reported in Table 1. The structure is subdivided into a stiffer center body and a flexible wing. Nine concentrated masses of 2 kg are equally spaced along the wing reference beam axis. The first ten in-vacuum natural frequencies of the test case and the classification of the corresponding mode shapes are reported in Table 2.

Unsteady aerodynamics is modeled using the Peters' finite-state unsteady airfoil theory [22] combined with a NACA0012 lookup table for determining the lift, drag, and pitching moment aerodynamic coefficient slopes at each point along the beam reference axis. A tip loss factor is applied to account for three-dimensional effects.

Table 2: Test case root-clamped in-vacuum natural frequencies.

Mode #	Mode type	Frequency (Hz)
1	Out-of-plane bending	2.19
2	In-plane bending	7.36
3	Out-of-plane bending	13.74
4	Out-of-plane bending	38.32
5	In-plane bending	46.75
6	Out-of-plane bending	66.25
7	Out-of-plane bending	88.19
8	Out-of-plane bending	95.45
9	In-plane bending	134.19
10	Torsion	134.77

4 RESULTS

The forecasting method is applied using strain output signals from various locations along the wing span. This choice is made because strains are independent variables used in UM/NAST and also structural variables directly measured in the practice. Output signals are obtained by simulating wing responses to a 1-cos vertical gust perturbation with maximum amplitude $w_{g_{max}} = 4$ m/s and duration $T_g = 0.1$, corresponding to a frequency $f_g = 10$ Hz. Gust responses are simulated up to $t = 30$ s with a time step $\Delta t = 5 \times 10^{-5}$ s. Strain outputs used for the forecasting are for the 4th and 8th vehicle elements that correspond to the wing-body intersection and the wing midspan (see the planform in Fig. 4). Strain variables are assumed to be constant throughout each element according to the UM/NAST strain-based structural formulation [14, 21].

Aeroelastic effects increase the frequency of the first aeroelastic mode such that it approaches the frequency of the second aeroelastic mode. This does not allow the effect of the CSD to be isolated from the output signals using a frequency-based filter, as was done in previous work on a cantilevered uniform high-aspect-ration wing [20]. Therefore, a modal decomposition is used in this work based on mode shapes identified via the ERA algorithm. This approach was previously used in a forecasting study of a typical section as reported in Ref. [13].

4.1 Baseline Model

The procedure for forecasting the bifurcation diagram is detailed considering the baseline test case at root angle of attack $\alpha = 0$ deg and without including the effect of self-weight. While this is not a practical flight condition, it is chosen for its simplicity and because the absence of statically nonlinear deformations allows to focus on the impact of dynamic nonlinearities. Thus, due to the vehicle symmetry with respect to the horizontal plane, no structural deformation occurs at $\alpha = 0$ deg when neglecting the weight, such that all gust perturbations are applied to the undeformed structure independently of the flight condition.

Forecasting the flutter speed and bifurcation diagram requires wing responses to perturbations at several speeds in the pre-flutter regime. Surrogate measurements are generated using UM/NAST as input to the forecasting method. In this example, system responses to gust perturbations at two speeds, $U = 158$ m/s and 159 m/s, before flutter are chosen as input to the forecasting algorithm. At each flow speed, a gust perturbation is applied to the wing. The wing response is recorded by collecting strain signals at several elements along the span and in dif-
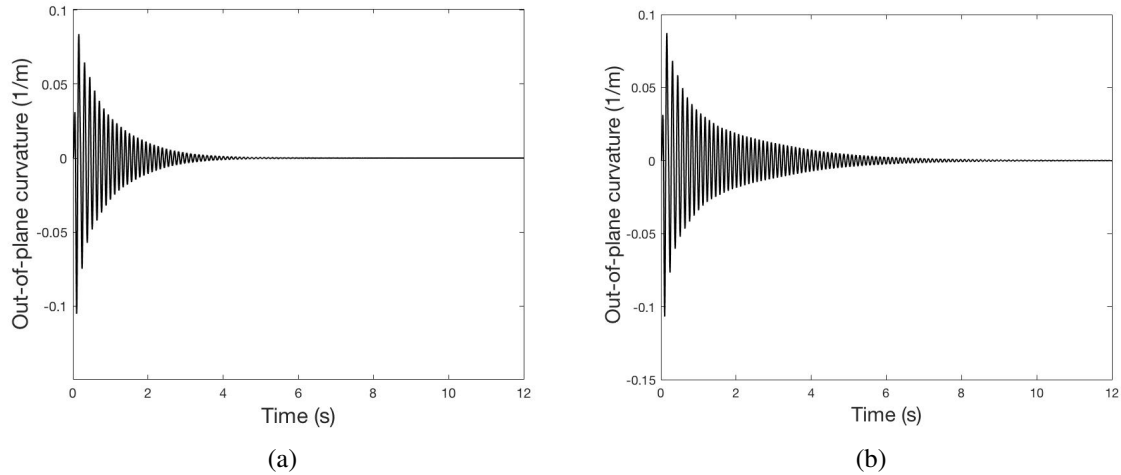
Figure 5: Wing recoveries from perturbations at (a) $U = 158$ m/s and (b) $U = 159$ m/s for the out-of-plane bending curvature recorded at the 8th element (wing midspan, see planform in Fig. 4).

ferent directions, i.e. considering the axial extension, torsional curvature, and out-of-plane and in-plane bending curvatures. As an example, the recorded gust response for the out-of-plane bending curvature at the 8th element (wing midspan, see planform in Fig. 4) and at $U = 158$ m/s and 159 m/s are shown in Fig. 5. These data and similar measurements recorded at several speeds in the pre-flutter regime are used as inputs to forecast the bifurcation diagram.

To build the bifurcation diagram of LCO amplitudes, local maxima and minima of the decomposed signals are used. Bifurcation diagrams for each recorded strain and at each element along the span can be forecasted separately. Following the forecasting procedure, curves of recovery rate of local maxima of out-of-plane bending curvature recorded at the 8th element (wing midspan, see planform in Fig. 4) are computed and shown in Fig. 6. Figure 7 (a) shows the forecasted bifurcation diagram constructed using the approximated recovery rates. The diagrams show the maximum and minimum amplitudes of the LCO as functions of speed. Forecasting results show that the system exhibits a subcritical bifurcation, where instability is possible even below the linear flutter speed. Reference LCO amplitudes for verification are shown in Fig. 7 using solid circles. These are obtained using time-marching to solve the nonlinear aeroelastic equations of motion in UM/NAST. To that aim, the system is perturbed at the corresponding speed and the equations of motion are time marched until the response converges to the stable LCO. Simulation results confirm the subcriticality of the flutter, and the linear flutter speed is approximated as 159.95 m/s. Results shows that the forecast diagram is in agreement with the reference values despite the fact that no information from the model is used in the forecasting. Furthermore, flutter is correctly identified to be subcritical. Using the same forecasting procedure, bifurcation diagrams for other strain variables at any element along the span can be obtained. As an example, bifurcation diagrams for torsional curvature recorded at the 8th element are forecast and shown in Fig. 6 (b).

4.2 Parametric Studies

The forecasting method is repeated by varying chosen design parameters. The goal is to demonstrate the method suitability for parametric studies and to investigate the impact of the chosen design parameters on the flutter type (subcritical or supercritical) and on the post-flutter LCO amplitude.
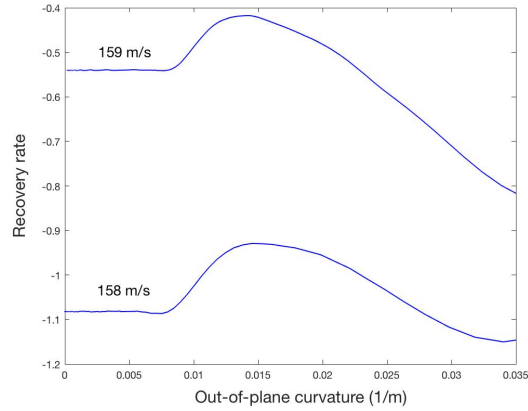
8

Figure 6: Recovery rate variation with amplitude obtained using local maxima of the signals shown in Fig. 5.
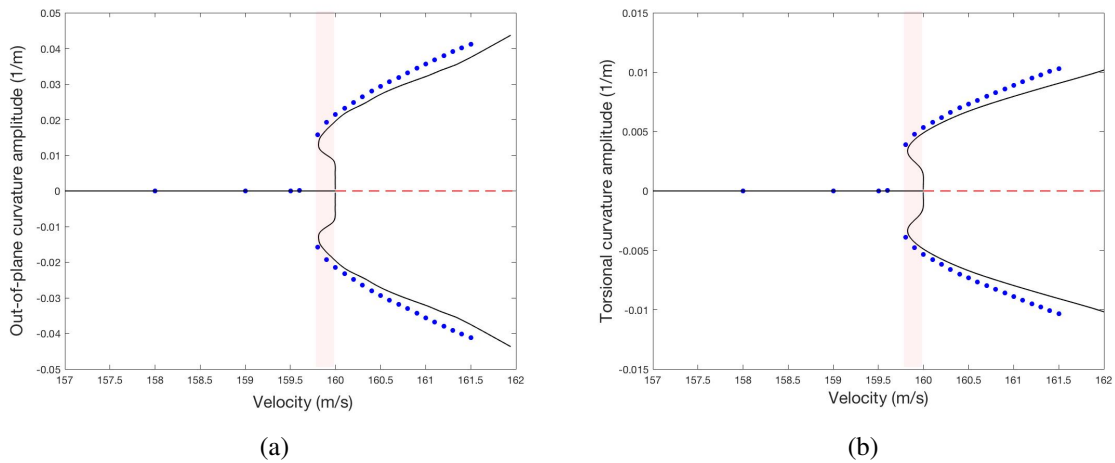

(a)

(b)

Figure 7: Bifurcation diagrams for (a) the out-of-plane bending curvature and (b) the torsional curvature at the 8th element (wing midspan). Solid lines are the forecasting results corresponding to the LCO amplitudes in the post-flutter regime. Solid circles show reference LCO amplitudes computed by direct nonlinear time-marching solutions. Shaded area shows the identified bi-stable region in the dynamics.

Parametric studies were conducted for $\alpha = 0$ deg and without including the effect for self-weight. In this situation, flutter occurs due to the coupling of out-of-plane bending and torsion motions with aerodynamics. Thus, parametric studies consider variations of the out-of-plane bending and torsion stiffness constants and of the wing sweep angle because these properties influence the degree of coupling between out-of-plane bending and torsion deformations. Properties are varied only in the wing (see planform in Fig. 4) while properties of the center body are not modified. For each set of new properties, bifurcation diagrams for all the elements along the wing span are constructed using as few as two measured wing gust responses. This capability demonstrates the advantages of the forecasting method for generating bifurcation diagrams of complex large-dimensional systems when the effect of several sets of parameters on the system dynamics needs to be studied.

Changes in the wing stiffness properties and sweep angle affect both the flutter point and the post-flutter bifurcation diagram. The variation in the flutter point prevents a direct comparison of the bifurcation diagrams because they are in different speed ranges. Therefore, speeds are normalized by the flutter speed of each parameter case such that bifurcation diagrams can be plotted on top of each other. For the sake of completeness, the relative variation in the flutter point (in terms of flutter dynamic pressure) with the out-of-plane bending and torsion stiffness constants and the sweep angle are reported in Tables 3 and 4. The variation is computed relatively to the flutter dynamic pressure of the baseline configuration equal to 9411.58 Pa. Flutter points are approximated by the forecasted bifurcation diagrams directly. As expected, increasing either the out-of-plane bending or torsion stiffness constants delays flutter, and a more pronounced effect is observed when increasing the torsion stiffness. When reducing the sweep angle from 30 deg (baseline configuration) to 15 deg flutter is anticipated, while it is delayed when further reducing the sweep angle to 5 deg. This behavior is caused by the different exchange of energy between the aeroelastic modes that originate from the first and third structural modes of the configuration when varying the sweep angle.

Figure 8 shows the bifurcation diagrams approximated for various uniform variations in the wing out-of-plane bending stiffness. Results are for the out-of-plane bending and torsion curvatures at the 4th and 8th elements (wing-body intersection and wing midspan, respectively, as shown in Fig. 4). Similar results can be plotted for other elements and strain variables as well. Bifurcation diagrams are computed for out-of-plane bending stiffnesses which are 10% and 20% greater and smaller than the ones of the baseline model. Results show that uniform changes in these properties throughout the wing span do not affect the flutter type, i.e. the bifurcation remains subcritical, while they impact the linear flutter speed as shown in Table 3. The post-flutter LCO amplitude is also affected by these stiffness variations. The degree of change in the LCO amplitude varies depending on the type of measured strain and the element location along the wing span. Results in Figs. 8 (a) and (c) show that reducing the out-of-plane bending stiffness slightly reduces the bi-stability region and the amplitude of post-flutter LCOs for the torsion curvature. However, this benefit comes at the cost of a lower linear flutter speed as shown in Table 3 and of a larger-amplitude LCO for the out-of-plane bending curvature shown in Figs. 8 (b) and (d). On the contrary, increasing the out-of-plane bending stiffness improves the linear flutter speed and reduces the amplitude of the out-of-plane bending curvature LCO, while it increases the LCO amplitude for the torsion curvature.

Figure 9 shows the approximated bifurcation diagrams for various uniform variations in the wing torsion stiffness. Trends are in line with the case of out-of-plane bending stiffness variations. Reducing the torsion stiffness anticipates flutter and increases the amplitude of LCOs for

Table 3: Variation in the flutter point with the out-of-plane bending and torsion wing stiffness constants.

	Flutter point variation			
Stiffness constant variation	-20%	-10%	10%	20%
Out-of-plane bending	-8.20%	-3.84%	3.28%	6.22%
Torsion	-13.04%	-6.27%	5.70%	11.04%

Table 4: Variation in the flutter point with the wing sweep angle.
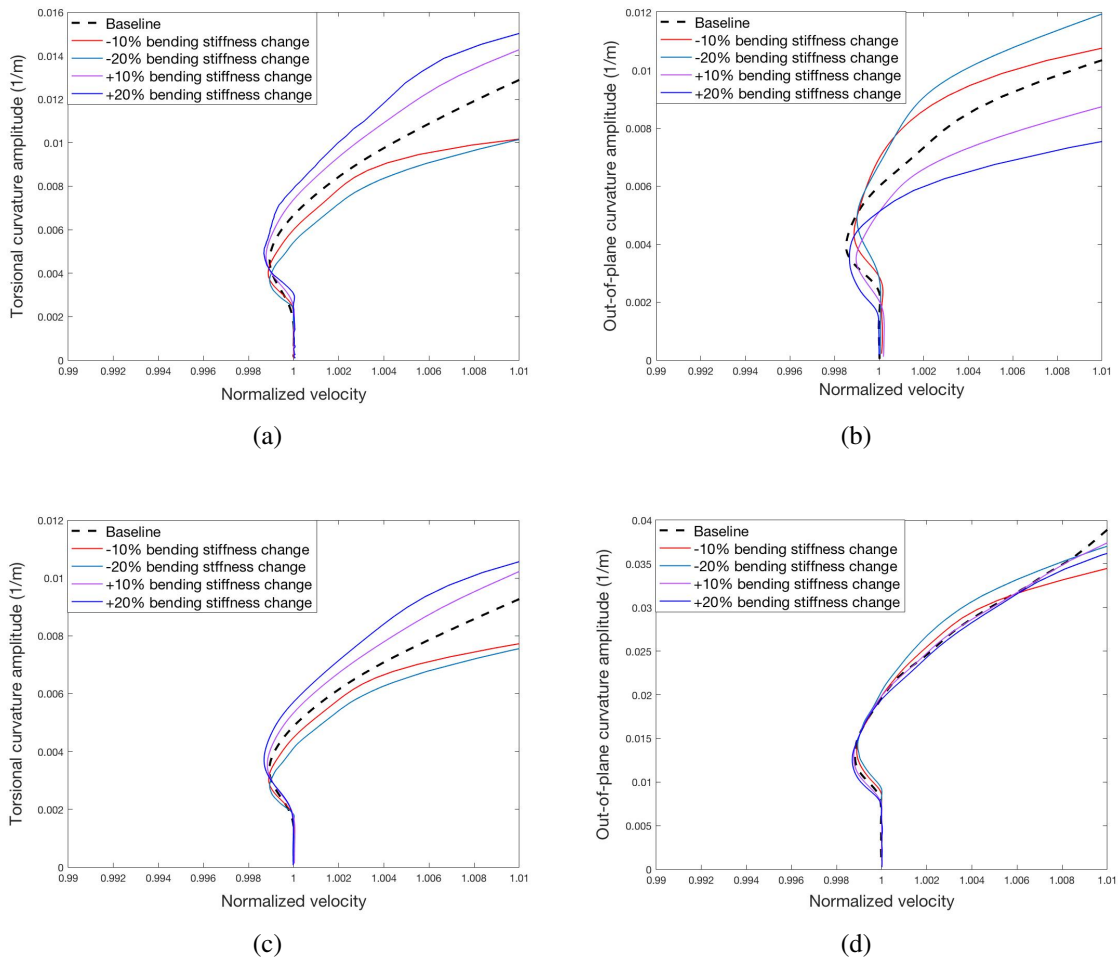
Sweep angle	Flutter point variation
15	-7.70%
5	5.54%

Figure 8: Variation in the bifurcation diagram with the wing out-of-plane bending stiffness for (a)-(b) the 4th element (wing-body intersection) and (c)-(d) 8th beam (wing midspan).
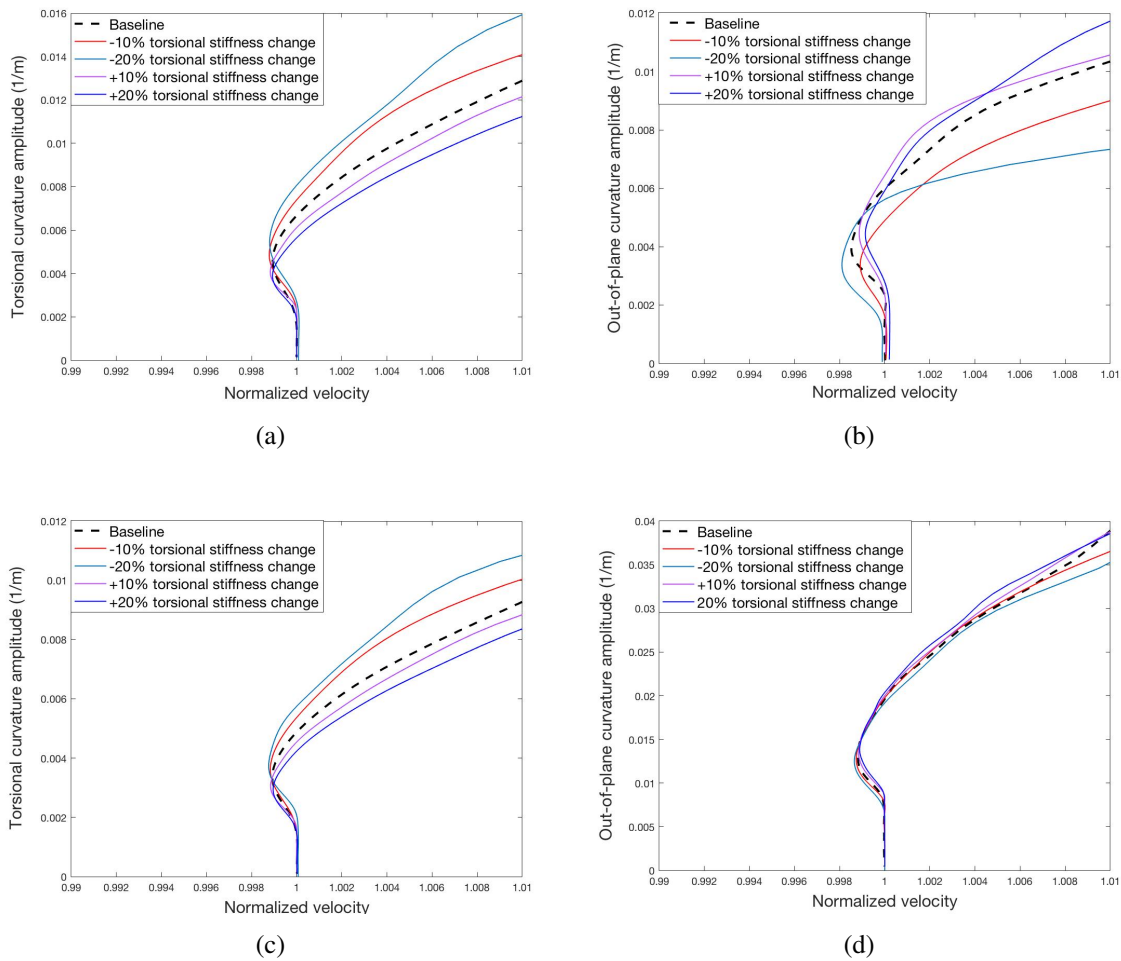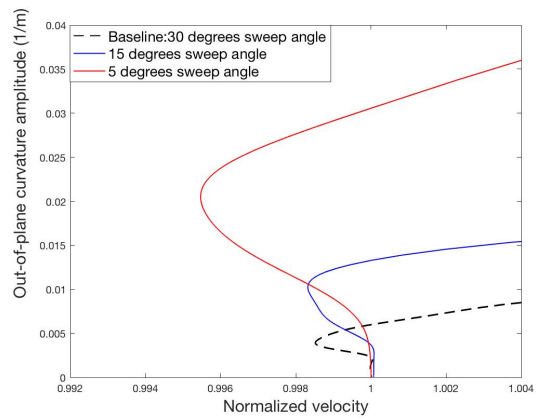
Figure 9: Variation in the bifurcation diagram with the wing torsion stiffness for (a)-(b) the 4th element (wing-body intersection) and (c)-(d) the 8th element (wing midspan).

the torsion curvature, while the amplitude of LCOs decreases for the out-of-plane bending curvature. These results suggest that when two deformations, i.e. out-of-plane bending and torsion, are coupled in the bifurcating mode, increasing the stiffness associated to one delays flutter but it increases the post-flutter LCO amplitude of the other. Contrasts between flutter point, flutter type, and post-flutter LCO amplitude were also observed in previous work on a subcritical, uniform cantilevered wing [23]. While such contrasts are not pronounced for the present test case and in the examined flight conditions, their possible occurrence is of great concern for design due to the need of ensure that flutter characteristics meet certification requirements.

Finally, Fig. 10 shows the bifurcation diagrams for variations in the wing sweep angle. The cases of sweep angles of 15 deg and 5 deg are considered as shown in Table 4, where the baseline wing has a sweep angle of 30 deg (see Fig. 4). Results show that modifying the wing sweep angle affects both the bi-stable region and the LCO amplitude in the post-flutter regime. Particularly, decreasing the sweep angle to 5 deg delays flutter but it increases the risk of jumping to a large-amplitude LCO before reaching the linear flutter speed due to the higher amplitude of the bi-stability region. This undesirable situation and the contrasts between flutter point and post-flutter LCO amplitude observed in the previous results highlight the need of developing efficient post-flutter analysis techniques for fast design space exploration of geometrically nonlinear configurations.
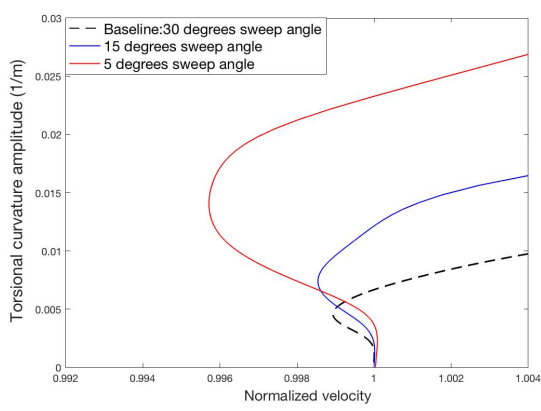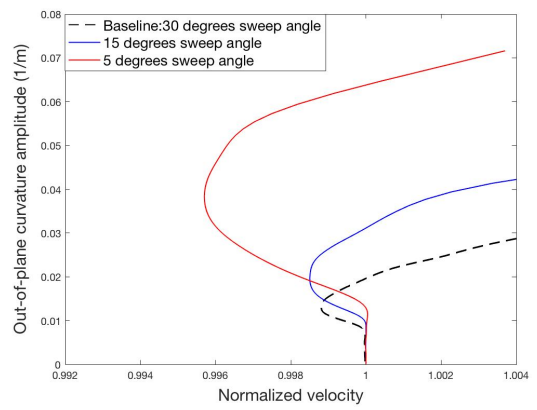
(a)

(b)
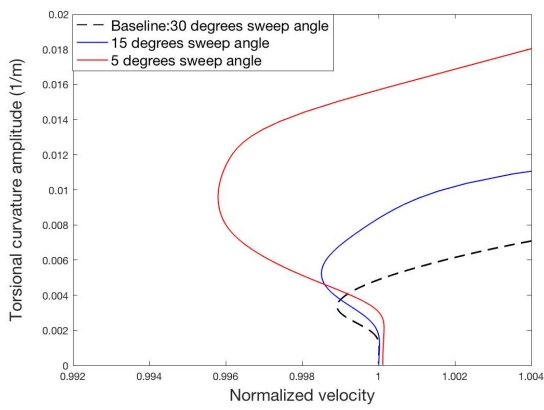
(c)

(d)

Figure 10: Variation in the bifurcation diagram with the wing sweep angle for (a)-(b) the 4th element (wing-body intersection) and (c)-(d) the 8th element (wing midspan).

5 CONCLUDING REMARKS

This paper demonstrates the suitability of a recently proposed model-free bifurcation forecasting method for investigating the post-flutter response of practical geometrically nonlinear aeroelastic systems. The method leverages the CSD phenomenon observed in nonlinear aeroelastic systems as they approach a flutter (Hopf) bifurcation to forecast the flutter point, flutter type (subcritical or supercritical), and the post-flutter bifurcation diagram. The method requires only few systems outputs collected in the pre-flutter regime with no need for computationally costly parameter sweeps or complex numerical continuation schemes, and it does not use information from a model of the system. These characteristics make it an effective approach for design space exploration of practical large-scale nonlinear aeroelastic systems such as geometrically nonlinear wings.

The method was applied to a half-vehicle BWB configuration assumed as clamped at the centerline. Output signals for the forecasting method were obtained by simulating gust responses using the UM/NAST framework, but no information from the UM/NAST model of the vehicle was used in the forecasting procedure. The test case was found to experience a subcritical flutter bifurcation with a narrow bi-stability region. The method accuracy was assessed by verifying the stable branch of the forecasted bifurcation diagrams against fully nonlinear time-marching simulations. Particularly, the method proved accurate in locating the folding point in the bifurcation diagram, that is, the lower limit of the bi-stability region. The knowledge of this point is of paramount importance for system experiencing subcritical bifurcations where limit cycle oscillations can arise even before reaching the flutter boundary.

Next, parametric variations in the wing out-of-plane bending and torsion stiffness constants and in the sweep angle were considered to investigate their impact on flutter and post-flutter characteristics and demonstrating the method suitability for design space exploration. Results pointed out contrasts between flutter point and amplitude of post-flutter response when uniformly varying the out-of-plane bending and torsion stiffness constants throughout the wing span. Furthermore, reducing the wing sweep angle was found to increase the amplitude of the bi-stability region. While the impact was small for the considered test case and flight conditions, the possible occurrence of undesirable subcritical LCOs before reaching the flutter boundary motivates the development of efficient post-flutter analysis methods for design space exploration of geometrically nonlinear aeroelastic systems.

6 REFERENCES

[1] Garrigues, E. (2018). A review of industrial aeroelasticity practices at dassault aviation for military aircraft and business jets. *Journal Aerospace Lab*, (14), 1–34.

[2] de C. Henshaw, M. J., Badcock, K. J., Vio, G. A., et al. (2007). Non-linear aeroelastic prediction for aircraft applications. *Progress in Aerospace Sciences*, 43(4), 65–137. doi:10.1016/j.paerosci.2007.05.002.

[3] Dowell, E., Edwards, J., and Strganac, T. (2003). Nonlinear aeroelasticity. *Journal of Aircraft*, 40(5), 857–874. doi:10.2514/2.6876.

[4] Jonsson, E., Riso, C., Lupp, C., et al. (2019). Flutter and post-flutter constraints in multidisciplinary design optimization. *Progress in Aerospace Sciences*, in press.

[5] Patil, M. J., Hodges, D. H., and Cesnik, C. E. (2001). Limit-cycle oscillations in high-aspect-ratio wings. *Journal of Fluids and Structures*, 15(1), 107–132. doi:10.1006/jfls.2000.0329.

[6] Tang, D. and Dowell, E. (1993). Experimental and theoretical study for nonlinear aeroelastic behavior of a flexible rotor blade. *AIAA Journal*, 31(6), 1133–1142. doi:10.2514/3.11738.

[7] Liu, L. and Dowell, E. H. (2005). Harmonic balance approach for an airfoil with a freeplay control surface. *AIAA Journal*, 43(4), 802–815. doi:10.2514/1.10973.

[8] Raghothama, A. and Narayanan, S. (1999). Non-linear dynamics of a two-dimensional airfoil by incremental harmonic balance method. *Journal of Sound and Vibration*, 226(3), 493–517. doi:10.1006/jsvi.1999.2260.

[9] Nayfeh, A. H. (2011). *The method of normal forms*. John Wiley & Sons.

[10] Vakakis, A. (1997). Non-linear normal modes (nnms) and their applications in vibration theory: an overview. *Mechanical Systems and Signal Processing*, 11(1), 3–22. doi:10.1006/mssp.1996.9999.

[11] Allgower, E. L. and Georg, K. (2012). *Numerical continuation methods: An introduction*, vol. 13. Springer Science & Business Media.

[12] Lim, J. and Epureanu, B. I. (2011). Forecasting a class of bifurcations: Theory and experiment. *Physical Review E*, 83, 016203–016203–9. doi:10.1103/PhysRevE.83.016203.

[13] Ghadami, A. and Epureanu, B. I. (2016). Bifurcation forecasting for large dimensional oscillatory systems: Forecasting flutter using gust responses. *Journal of Computational Nonlinear Dynamics*, 11, 061009–061009–8. doi:10.1115/1.4033920.

[14] Su, W. and Cesnik, C. E. S. (2010). Nonlinear aeroelasticity of a very flexible blended-wing-body aircraft. *Journal of Aircraft*, 47(5), 1539–1553. doi:10.2514/1.47317.

[15] Strogatz, S. H. (2001). *Nonlinear Dynamics and Chaos with Application to Physics, Biology, Chemistry, and Engineering*. Westview Press, 1st ed.

[16] Lim, J. and Epureanu, B. I. (2012). Forecasting bifurcation morphing: application to cantilever-based sensing. *Nonlinear Dynamics*, 67(3), 2291–2298. doi:10.1007/s11071-011-0146-8.

[17] Ghadami, A. and Epureanu, B. I. (2017). Forecasting the post-bifurcation dynamics of large-dimensional slow-oscillatory systems using critical slowing down and center space reduction. *Nonlinear Dynamics*, 88, 415–431. doi:10.1007/s11071-016-3250-y.

[18] Ghadami, A. and Epureanu, B. I. (2018). Forecasting critical points and post-critical limit cycles in nonlinear oscillatory systems using pre-critical transient responses. *International Journal of Non-Linear Mechanics*, 101, 146–156. doi:10.1016/j.ijnonlinmec.2018.02.008.

[19] Yamasaki, H. and Epureanu, B. I. (2017). Forecasting supercritical and subcritical hopf bifurcations in aeroelastic systems. *International Journal of Non-Linear Mechanics*, 94, 400–405. doi:10.1016/j.ijnonlinmec.2016.12.009.

[20] Ghadami, A., Cesnik, C. E. S., and Epureanu, B. I. (2018). Model-less forecasting of hopf bifurcations in fluid-structural systems. *Journal of Fluids and Structures*, 76, 1–13. doi:10.1016/j.jfluidstructs.2017.09.005.

[21] Su, W. and Cesnik, C. E. S. (2011). Strain-based geometrically nonlinear beam formulation for modeling very flexible aircraft. *International Journal of Solids and Structures*, 48(16-17), 2349–2360. doi:10.1016/j.ijsolstr.2011.04.012.

[22] Peters, D. A., Hsieh, M. C. A., and Torrero, A. (2007). A state-space airloads theory for flexible airfoils. *Journal of the American Helicopter Society*, 52(4), 329–342. doi: 10.4050/JAHS.52.329.

[23] Stanford, B. and Beran, P. (2013). Direct flutter and limit cycle computations of highly flexible eings for efficient analysis and optimization. *Journal of Fluids and Structures*, 36, 111–123. doi:10.1016/j.jfluidstructs.2012.08.008.

COPYRIGHT STATEMENT